A Cloudiness Transition in a Marine Boundary Layer

ALAN K. BETTS

Middlebury, Vermont

REINOUT BOERS*

NASA/Goddard Space Flight Center, Greenbelt, Maryland

ABSTRACT

In situ aircraft data and lidar data are used to analyze a transition in the boundary layer thermodynamic structure from a clear boundary layer through small cumulus and broken stratocumulus to a deck of solid stratocumulus. The data was collected in conjunction with a Landsat overpass on 7 July 1987 off the coast of southern California. A steady progression in mixing line stability is seen associated with the change in cloudiness. The (empirically based) stability threshold for the breakup of this stratocumulus is that the slope of the mixing line is 0.66 ± 0.04 of the slope of the wet virtual adiabat (the stability threshold for cloud-top entrainment instability). We propose a simple linear parameterization for cloud fraction in terms of mixing line stability. Surface flux measurements are consistent with bulk aerodynamic estimates. We present mean profiles for the four cloudiness regimes for further analysis.

1. Introduction

Boundary layer cloudiness plays several important roles in the energy budget of the earth. Low level stratocumulus are highly reflective clouds which reduce the net incoming shortwave radiation at the earth's surface. They are found over the cooler water of the Eastern oceans bordering the continent (Lilly 1968; Schubert et al. 1979, Albrecht et al. 1985). Climatically, the transition to a small area fraction of scattered cumulus clouds occurs as the air flows over warmer water. Although these clouds reflect less sunlight, they cover a larger area, and play an important role in the boundary layer equilibrium by transporting water vapor upwards, and enhancing the surface evaporation (Betts 1986; Betts and Ridgway 1989). The First ISCCP (International Satellite Cloud Climatology Project) Regional Experiment (FIRE) included a marine stratocumulus experiment off the southern California coast from 29 June to 19 July 1987 (Randall et al. 1984; Albrecht et al. 1988). The objectives of this experiment included the study of the controls on fractional cloudiness, and the assessment of the role of cloud-top entrainment instability (Randall 1980; Deardorff 1980) and mesoscale structure in determining cloud type. The strategy was to collect in situ measurements using re-

search aircraft, balloon and sounding systems located on San Nicolas Island, together with simultaneous satellite observations, so that the results could be integrated into the overall ISCCP objective of monitoring cloud fields from space.

The focus of this paper is one research day, 7 July 1987, which provided a valuable data set to address many of the objectives. Coordinated aircraft missions were flown by four research aircraft, the National Aeronautics and Space Administration (NASA) ER2 and the University of Washington C-131, the National Center for Atmospheric Research (NCAR) Electra, and the British Meteorological Office C-130 research aircraft, centered on a Landsat scene at about 1800 UTC. The remarkable feature of this Landsat scene (Fig. 1) is the transition from a clear sky in the west through tiny cumulus and broken stratocumulus to solid stratocumulus in the east. In this paper, we shall analyze the dynamic and thermodynamic structure of this transition in cloudiness using data from the NCAR Electra. Around the time of the Landsat scene, the Electra flew a butterfly pattern at 2100 m to map the cloud fields with a downward looking lidar and radiometers (Fig. 2). Immediately afterwards, the Electra flew an east–west line pattern through the cloud layer, 120–150 km in length centered on the boundary between the stratocumulus and cumulus, which was moving eastwards at 3 m s^{-1}. By averaging the aircraft data, we shall document the internal structure of the different cloud regimes, and show that the transition between broken cumulus and stratocumulus is asso-

---

* Affiliated with University Space Research Association.

Corresponding author address: Dr. Alan K. Betts, RD2, Box 3300, Middlebury, VT 05753.

ciated with a distinct change in thermodynamic structure: namely towards a more stable mixing line. However, this results in this case not simply from a decrease in sea surface temperature, but mostly from an increase in the strength of the inversion capping the boundary layer. The data suggest a new thermodynamic stability criterion for the transition between stratocumulus and cumulus, one which is more unstable than the cloud-top entrainment instability (CTEI) criterion.

The earliest reference to the CTEI-condition was Lilly (1968) who suggested that unstable downward mixing would produce stratocumulus breakup if there were a decrease of equivalent potential temperature, θ_e, upward through the capping inversion. Randall (1980) and Deardorff (1980) considered liquid water loading and formulated CTEI in terms of a jump condition at cloud top. They found the instantaneous jumps in equivalent potential temperature and mixing ratio at the top of the cloud layer that were necessary in order for the cloud to remain thermodynamically stable. Later studies by Mahrt and Paumier (1982), Hanson (1984, 1987), Randall (1984), Albrecht et al. (1985), Nicholls and Turton (1986), Kuo and Schubert (1988), and Siems et al. (1990) have refined the original condition, and examined mixing process at the cloud top which include unsaturated as well as saturated parcels. Betts (1982, 1983) introduced saturation point diagrams in which this idealized CTEI criterion can be graphically identified as the slope of the wet virtual adiabat. An advantage of this method is that it eliminates the necessity to define jumps in thermodynamic variables at the cloud top. In Appendix A, we briefly review this method, using the θ^*-q^* diagrams presented in this paper.

2. Experimental design and data processing

a. Data collection on 7 July 1987

The Landsat scene in Fig. 1 is near 1800 UTC. The width of the scene is about 180 km. The Electra flight legs are summarized in Table 1. There is a descent sounding from the ferry altitude of 3000 m (700 hPa) to 2100 m (790 hPa) where a butterfly pattern was flown centered on the Landsat scene. As well as flight level data, a downward looking lidar mapped cloud top. The times at selected points are shown on Fig. 2. At 1851 UTC, the Electra made a descent sounding to 50 m (1010 hPa), followed by an east–west run at that altitude along latitude 31.6°N (centered on the cloud transition boundary in Fig. 1) to measure the sea surface temperature (using a downward looking radiometer), low level fluxes (using a gust probe) and flight level data. Successive level runs were made (see Table 1) across the cloud transition boundary (which moved slowly eastward from about 121.91° to 121.58°W during the pattern time) at 335 m (975 hPa), and 550 m

(950 hPa); followed by a sounding leg with continuous ascent and descent from cloud base up through the inversion; another level leg above the clouds at 1400 m (860 hPa); and a final leg back near the surface at 50 m. Additional soundings were taken at the ends of this pattern and the return flight. The processing and correction of the Electra data is discussed in section 2c. The averaging of the data to give a mean description of four different cloud regimes (stratocumulus, broken stratocumulus, cumulus and the cloud free region to the west) is outlined in section 4.

b. Meteorological conditions

On the synoptic scale, Fig. 3 shows the National Meteorological Center analysis of the surface pressure at 2100 UTC 7 July, close to the central time of the aircraft pattern. The center of the surface subtropical high pressure system is located near 35°N, 140°W with a ridge protruding northeastward into the Pacific Northwest. The protrusion was weaker than on previous days as a surface low pressure system approached the southern coast of British Columbia. Cloudy conditions and light southeast winds prevailed along the Washington–Oregon coast with scattered light precipitation falling at many locations as a storm system approached. The 500 hPa flow (Kloessel et al. 1988) was nearly zonal as a trough located on the U.S. West Coast continued to weaken and move inland.

Between the subtropical high pressure system (further south and east than earlier in the experiment) and the thermal trough along the Arizona–Mexico border there is a tight pressure gradient over the FIRE region, resulting in strong north-northwesterly winds of ≈ 10–15 m s^{-1}. The 850 and 700 hPa high pressure centers (not shown) were located directly above the surface high pressure system, giving strong north-northwesterly winds up to 700 hPa. Winds along the California coast were also northwesterly but weaker (2–5 m s^{-1}). The offshore flow over the Washington–Oregon coastal areas appeared to contribute to a large clear region just offshore that formed on 6 July 1987 and proceeded to move southward into the FIRE region on 7 July 1987.

Detailed cloud photography and observers notes indicate that only the far northwestern region of the Landsat scene was completely cloud free. Further east, clouds first appeared as small puffs of cumulus in streets along the mean wind, followed by larger flat isolated cells. In the eastern part of the flight area these cells had merged to form a nearly solid stratocumulus layer. This transition in cloudiness was accompanied by significant changes in the mean wind (shear), temperature and moisture structure as will be discussed below. The Landsat cloud picture (Fig. 1) shows in the stratocumulus towards the east roughly linear cloud structures, oriented with the mean boundary layer wind, with small breaks spaced about 10 km apart. Inside these larger structures smaller scale structures occur on all
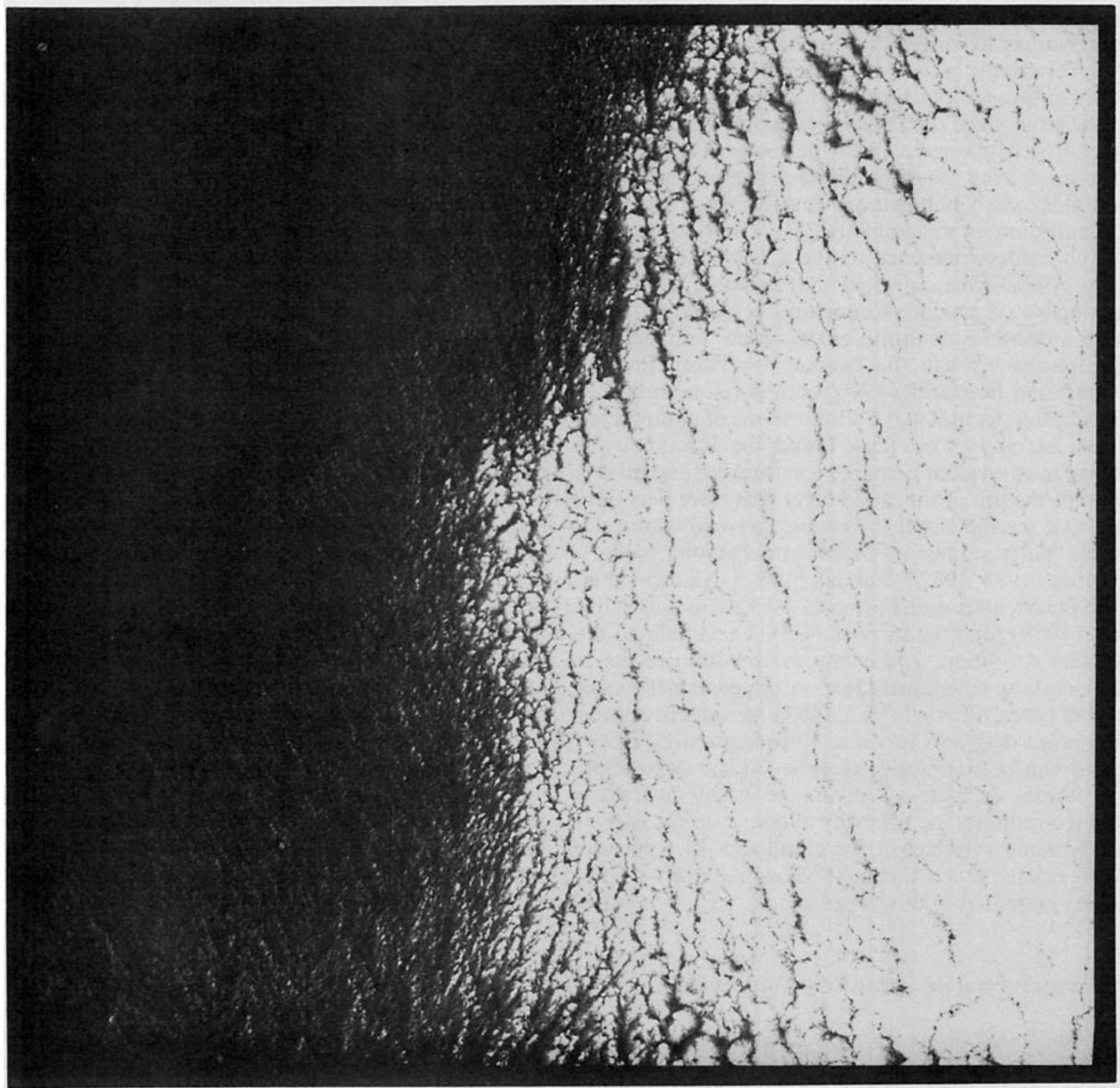
FIG. 1. Landsat scene at 1830 UTC 7 July 1987 with center coordinates 33°10'N, 121°44'W.

scales down to the 30 m Landsat resolution, though the smaller scale variations are not evident in the exposure shown here. This turbulence structure reflects variations in the integrated liquid water, which has been shown to obey a $k^{-5/3}$ wavenumber spectrum for scales larger than the cloud thickness, due to the two-dimensional upscale cascade of energy generated at the cloud thickness scale (Cahalan and Snider 1989; Lilly 1989).

c. Data processing and correction

In order to derive a consistent thermodynamic dataset including air parcel saturation point for clear and cloudy air (Betts 1982), the quality of the instrumental output had to be carefully evaluated. The critical instruments are the temperature and humidity sensors. Temperature was measured by four sensors: a Rosemount sensor (model 102) located on the boom sensor (ATB1), NCAR's fast response sensor (K-probe, ATKP1), NCAR's reverse flow sensor (ATRF1) and a near-field radiometer (a PRT6). This last sensor probes a volume of air remotely and cannot be used to measure parcel temperature. A comparison of the first three sensors showed that each had a consistent offset with respect to the others. The ATKP1 showed the highest readings. The ATRF1, ATB1 had relative offsets of −0.4°C, −0.9°C respectively. A comparison of incloud flight leg data sections with the PRT6 (which
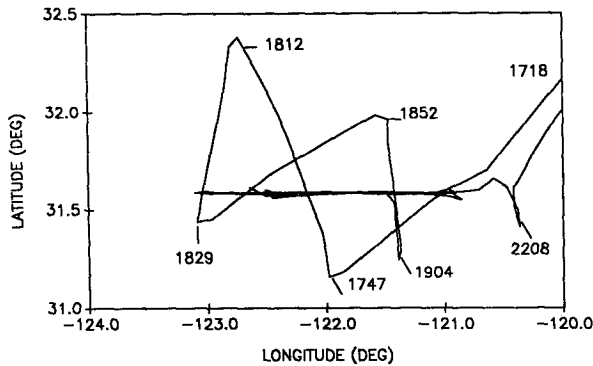
FIG. 2. Patterns flown by NCAR Electra 7 July 1987.

is unaffected by probe wetting) revealed a significant evaporative cooling for both the ATKP1 and the ATRF1 due to apparent wetting by cloud particles. Some wetting of the ATRF1 was observed, although this instrument is designed to reduce this problem. After cloud exit it took these instruments two to three seconds to recover. In consequence we chose to use the ATB1 temperature sensor, because it was least affected by wetting.

Dewpoint was measured by two EG&G Model 137 hygrometers (DPBC, DPTC) and by a fast-response Lyman-alpha (L-A) hygrometer. Absolute humidity from the L-A probe is obtained from a coupling of its output voltage to one of the dewpoint sensors (DPTC in this case). The dewpoint sensor was affected by wetting of the mirror in cloudy regions. The dewpoint sensors are well known for their slow response to rapid humidity variations (Duchon and Goerss 1976; Boers and Betts 1988), and spurious oscillations and variable instrument response. Typical offsets between the DPTC and the DPBC are $1\,°C$ for dewpoint values between $0°$ and $10\,°C$ up to $6\,°C$ for dewpoints around $-15\,°C$. Preprocessing of the dewpoint data included a three-second averaging and a time shift of two seconds to approximately account for the slow response time (see
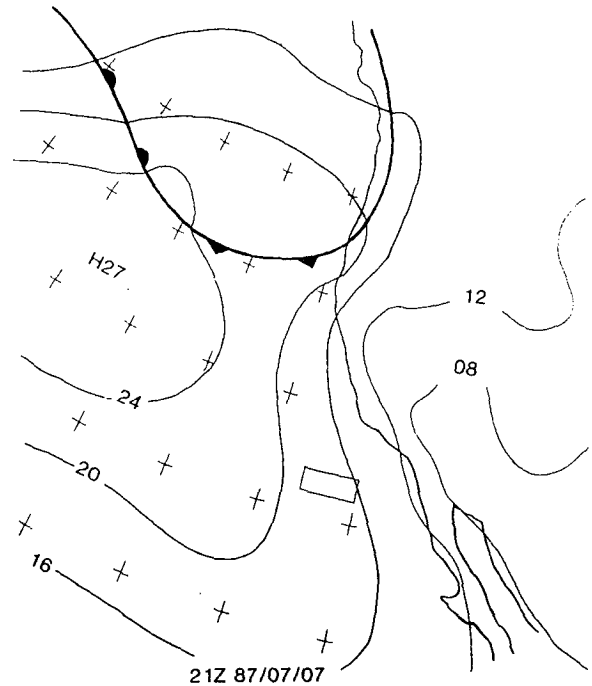

FIG. 3. Surface meteorological conditions
at 0000 UTC 8 July 1987.

Boers and Betts 1988, for details). Next, profiles of potential temperature and dewpoint were examined for matching data sections in cloudy regions. Due to the probe wetting problems with the ATKP1 and the ATRF1 it was decided that only the ATB1 could be used to derive the saturation point values, and either the DPTC or DPBC for humidity. We chose the DPTC with an offset of $0.4\,°C$ to match the ATB1 in clouds.

The liquid water data was taken from the PMS–FSSP probe, and is an integration over the channels in which the number of particles are collected. This measurement was chosen over the other liquid water probes, which suffered from variable offset problems. Typical error in liquid water is $\pm50\%$, and there is a tendency for the liquid water to be underestimated.

For all temperature and moisture data we computed the saturation level quantities liquid water potential temperature θ^*, total water mixing ratio, q^*, and equivalent potential temperature θ_e^*. Errors in liquid water content shift saturation level quantities parallel to lines of constant θ_e^*. Fortunately liquid water contents are low, and only one leg is fully in cloud in the stratocumulus region, so our results are not sensitive to the uncertainties in the liquid water measurements.

3. West–east cross sections

In this section we discuss the horizontal gradients at the sea surface and in the CBL across the cloudiness transition and compare the fluxes measured at the low-

TABLE 1. Electra flight legs on 7 July 1987.

Pattern	Altitude (m)	Altitude (hPa)	Time (UTC)
Sounding	3000–2100	700–790	1729–1735
Butterfly	2100	790	1735–1851
Sounding	2100–50	790–1010	1851–1909
Turbulence leg	50	1010	1911–1933
Sounding	50–1500	1010–850	1933–1941
Turbulence leg	335	975	1941–2010
Turbulence leg	550	950	2014–2037
Sounding	550–1500	950–850	2037–2042
Sounding leg	460–1400	960–860	2042–2105
Lidar leg	1400	860	2110–2131
Sounding	1400–50	860–1010	2132–2137
Turbulence leg	50	1010	2137–2154
Sounding	50–1500	1010–850	2154–2159

est aircraft level with estimates using bulk aerodynamic fluxes.

a. Determination of sea surface pressure and temperature

Several methods were attempted to compute the sea surface pressure. Accurate values are necessary for the computation of the sea surface potential temperature and saturation mixing ratio for our conserved variable analysis, and to compare a bulk aerodynamic estimate of the surface fluxes with those measured by gust probe at the lowest flight level. Our first method consisted of averaging the sea surface pressure values as derived from the NCAR-Electra aircraft tapes. These computations are based on an assumption (supported by Fig. 12, see later) that the virtual potential temperature below the aircraft flight level is constant, so that the surface pressure can be inferred from a simple integration of the hydrostatic equation. Inconsistent results were found when different flight legs and levels were compared. Variations of as much as 3 hPa between flight legs were deemed too much to use this data to determine the average pressure. However horizontal pressure gradients showed consistent variations; approximately a 1.2 hPa increase in pressure from east to west over a 1 degree longitude interval. This is comparable to the large-scale pressure gradient. Our second method consisted of extrapolating the pressure versus radar altitude plot to the surface. In the averaging for the four regions we were hampered here by the absence of part of the vertical profiles in some of the regions (particularly the "Cumulus" region to the west) so that surface pressure extrapolation suffered from an uncertainty of 1–2 hPa. We decided to retain the gradients in average sea surface pressure as observed from the computation in the first method, and use a mean sea surface pressure of 1017.5 hPa consistent with surface synoptic charts.

For the sea surface temperature we used the radiometric temperature as derived from the downward looking radiometer corrected for sea surface reflection of sky longwave radiation. An estimate of the sky radiation was available from the upward looking radiometer. The sea surface potential temperature was then computed using the corrected sea surface temperature and a sea surface pressure of 1017.5 hPa with a superimposed east–west gradient of 1.2 hPa/deg (long). The mixing ratio at the surface was computed by assuming saturation at the sea surface.

b. Gradient of sea surface temperature

Figure 4 shows the sea surface temperature (SST) cross section determined from three flight legs, the two lowest legs at about 70 m and the third in the subcloud layer near 400 m (975 hPa). The position and time of the broken cloud transition region at the time of the first and last legs at 1010 hPa is marked: (See section
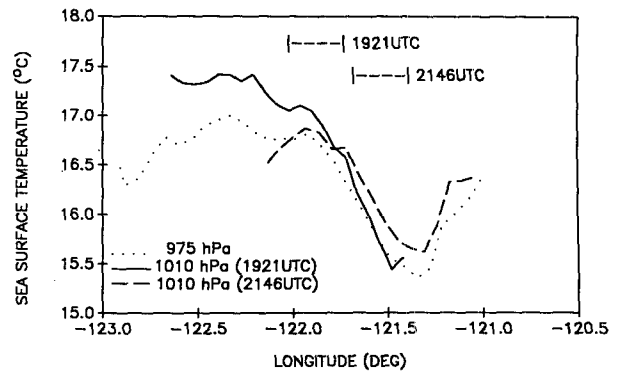

FIG. 4. Sea surface temperature gradient.

4.) The SST is lower on the stratocumulus side to the east by about 1 °C although further to the east the SST increases again. The radiometric estimate of the surface temperature from the higher flight level is systematically 0.2°C lower in the eastern part of the leg, but to the west the discrpancy seems larger for reasons unknown. Satellite estimates in the cumulus portion are also negatively biased, but mainly due to inability to resolve the small fair weather cumulus. Landsat, which does resolve most cumulus, has only a 0.85°C bias, while 1 km AVHRR estimates are biased by 2.17°C compared to the aircraft (Cahalan and Snider 1989). We simply averaged all values in 0.05° longitude bins to get a mean east–west SST cross section and then computed a θ cross section using the sea surface pressure gradient.

c. Horizontal gradients near the surface, and the surface fluxes

Figure 5a shows the west–east cross section of mean θ for the sea surface and the average θ of the two runs at 1010 hPa. To the west in the cumulus and clear regions there is a positive sea–air θ difference, while under the stratocumulus in the east there is a reversal because of the large drop of SST. Figure 5b shows the corresponding difference of mixing ratio between the surface (a saturation value) and 1010 hPa. Figure 5c shows the cross section of mean wind speed, V, measured by aircraft at 1010 hPa. Wind speeds are much higher on the stratocumulus side. We computed sensible and latent heat fluxes (H_S, H_L) using the bulk aerodynamic method, and differences between the surface and 1010 hPa.

$$H_S = \rho C_p C_T V_{1010}(\theta_0 - \theta_{1010}) \qquad (1a)$$

$$H_L = \rho L C_T V_{1010}(q_{s0} - q_{1010}) \qquad (1b)$$

where the subscript 0 denotes an ocean surface value. We used a constant transfer coefficient of $C_T = 1.0 \times 10^{-3}$, which is a compromise between slightly higher values for the unstable conditions to the west, and
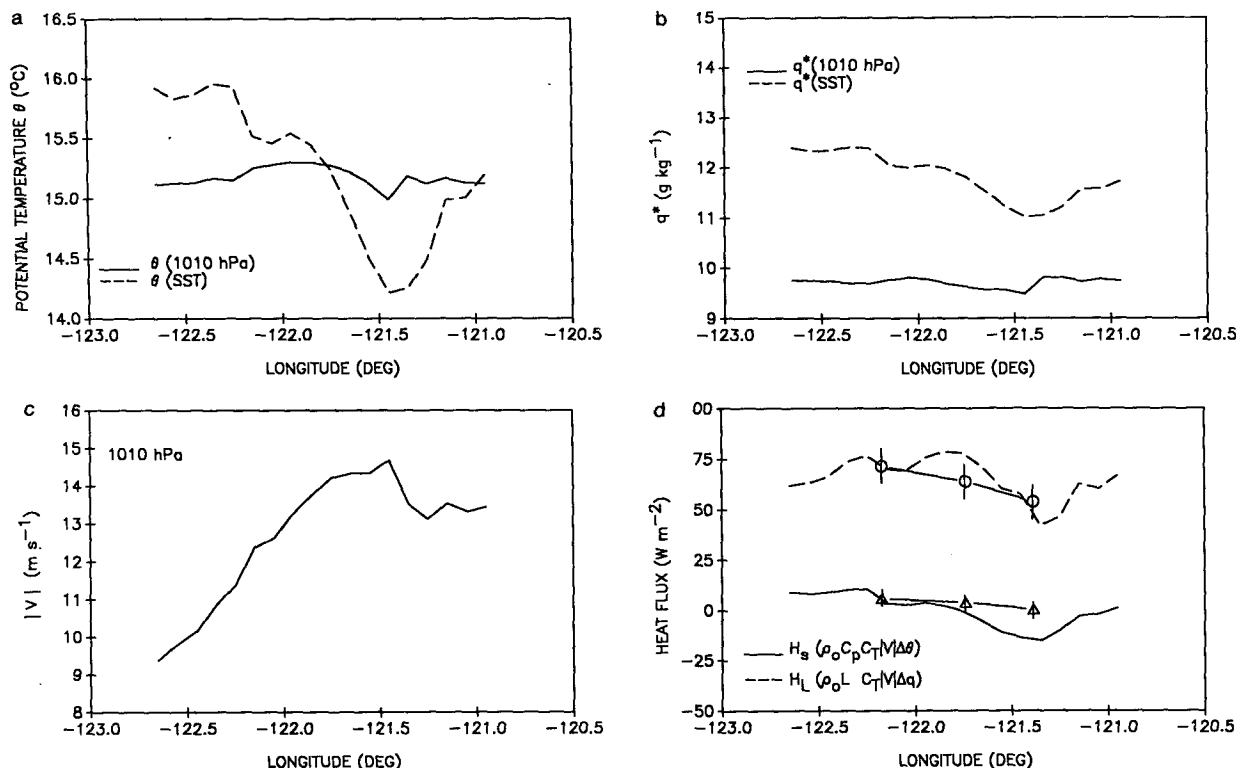
FIG. 5. Cross section (a) of θ and (b) of q for sea surface and 1010 hPa; (c) cross section of mean 1010 hPa wind. (d) Comparison of bulk aerodynamic fluxes and fluxes measured by aircraft.

slightly lower values for the more stable conditions to the east. Figure 5d compares these bulk fluxes estimated from (1) with those measured with the gust-probe system on the Electra (Albrecht 1989, personal communication). Figure 5d shows that the surface latent heat flux decreases across the cumulus–stratocumulus transition, and the surface sensible heat flux falls to near zero or becomes negative.

The Electra values are averages for the three regions discussed in the next section: cumulus plus clear, transition and stratocumulus. The agreement is satisfactory, considering the number of independent measurements being combined here; the residual uncertainties in the sea surface pressure and temperature, and our corrections to the Electra temperature and dewpoint observations. Error bars for the Electra fluxes measured by the gust-probe and Lyman-alpha system are shown. The bulk aerodynamic fluxes depend on the radiometric measurement of SST (accuracy ±0.2 K see Fig. 4), and our correction to the dewpoint (+0.4 K), and any unknown bias in the slow response air temperature. An error of 0.4 K in the SST, or air temperature gives an error of 5 W m^{-2} in H_s, and the same error in SST or dewpoint gives a 9 W m^{-2} error in H_L. An error of 2 hPa in the surface pressure gives an error of 2.5 W m^{-2} in H_s, but ≤0.5 W m^{-2} in H_L. The agreement in Fig. 5d gives us confidence that our corrections to the

data discussed in the previous section have probably reduced the relative temperature biases to ≤0.4 K, the dewpoint biases to ~0.4 K, and the surface pressure error to ≤2 hPa.

d. Aircraft cross sections in the CBL

Figures 6a and 6b show the four cross sections of saturation potential temperature of θ^* (θ, except for the in-cloud parts of the 950 hPa leg), and q^* (total water) within the CBL. Figure 6a again shows the two runs at 1010 hPa for the earliest leg centered at 1921 UTC (1121 PST) and for the last leg centered at 2146 UTC (1346 PST). There is a considerable change ($\approx$0.25 K in θ, and $\approx$0.5 g kg^{-1} in q) during this 2.5 hours with a warming and moistening at all longitudes. We cannot readily assess how much of this may be advection, and how much local change due in part to solar absorption near local noon. Betts (1989) found a considerable diurnal cycle in two days of boundary layer soundings from San Nicolas Island with a subcloud layer warming of 1.2 K in a six hour period from 0800 to 1500 PST. The warming rate shown in Fig. 6a over 2 hours is comparable. At the 950 hPa level, Figs. 6a and 6b show the strong gradients within the inversion, which is lower on the western (cumulus) side.
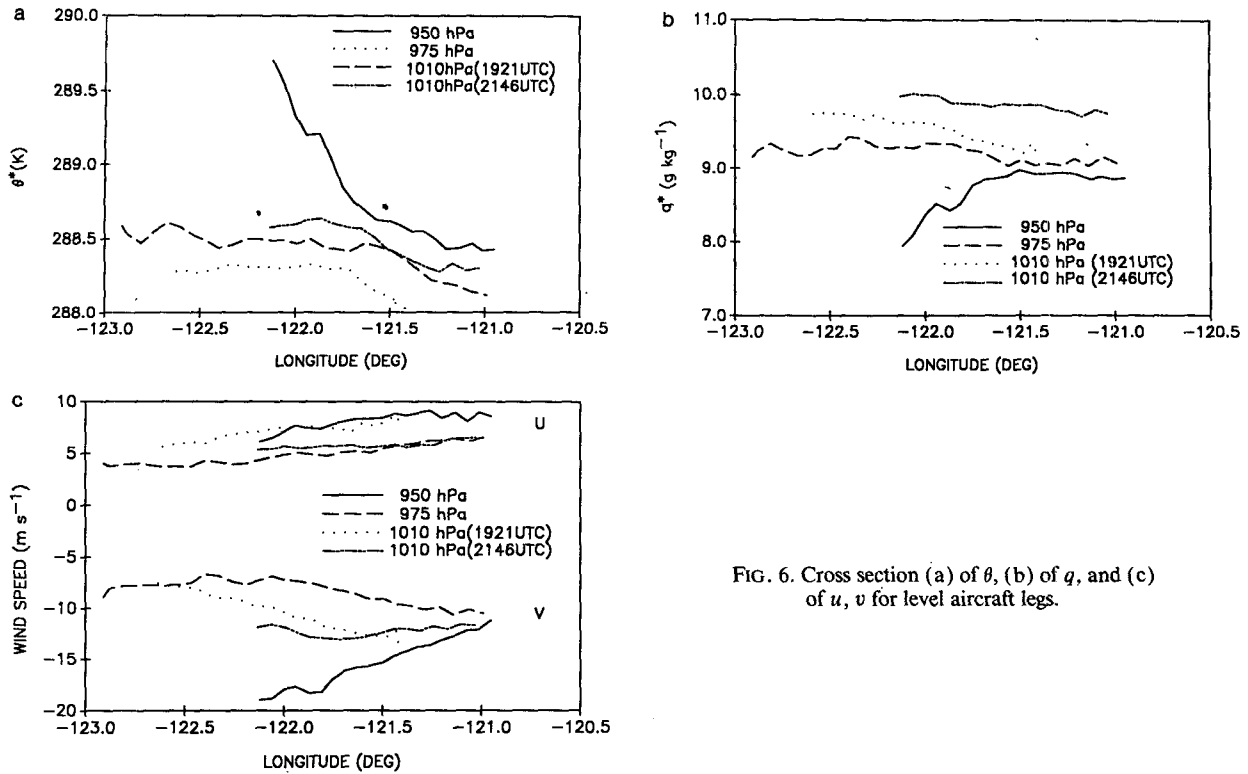
FIG. 6. Cross section (a) of θ, (b) of q, and (c)
of u, v for level aircraft legs.

The low level east–west gradients roughly follow the trend of SST as might be expected. The warming and moistening with time present a possible analysis problem. The legs at higher levels (975, 950 hPa, and above) are all at intermediate times, so we decided to average the two lowest level legs and construct a single mean picture (see section 4) representative of the central time (2032 UTC). We attempted other partitions of the data into early and late time blocks, but there is insufficient sampling to do this: The aircraft pattern took the 2.7 hours to fly and the lowest level leg was the only one repeated.

Figure 6c shows corresponding cross sections of the u and v components for the three low levels. The general flow is from the northwest at 10–15 m s^{-1}. The u component is about 6 m s^{-1} and it weakens slightly with time at 1010 hPa. In the first 1010 hPa aircraft leg the northerly component in the west under the cumulus is weaker ($\sim$8 m s^{-1}) than for the last 1010 hPa leg. The aircraft legs were moved to the east, to follow the cloud transition boundary (see section 4). Under the stratocumulus, the wind speed is stronger from the northwest ($\sim$12 m s^{-1}). The boundary between cumulus and stratocumulus appeared to move at $\sim$3 m s^{-1}, while the u wind component in the CBL is near 6 m s^{-1} (Fig. 6c), so there is an advection towards the east relative to the surface of $\sim$50 km (0.5° in longitude), and an apparent advection of half this (25 km) relative to the cloud transition boundary between the first and last runs. However the advection

from the north is strong and the cloud transition boundary has structure in the north–south direction (see Fig. 1), so we cannot accurately assess the relative flow across the cloud boundary. All the runs below cloud base (1010 and 975 hPa) show a gradient of θ and q with higher values to the west under the cumulus (where the SST is higher: see Fig. 4), so the shift in Fig. 6a, of the steepest gradient in θ towards the east appears to be partly advective.

e. Lidar observations

The NCAR Airborne Infrared Lidar System (NAILS) was operated during FIRE. NAILS is equipped with a rotating mirror used to obtain range to cloud boundary in either the upward or downward looking mode. Because of the long wavelength (10 micron) this lidar system is only sensitive to large particles and was not used to detect aerosol information. Detailed information about the design of NAILS is given in Schwiesow (1987). The system was used in the pulsed mode at a repetition rate varying between 8 and 16 Hz. Two shots were averaged so that 4 to 8 laser shots per second were available to extract the cloud height information. The selected lidar profiles analyzed here were taken at the 8 Hz rate so that a 15 m resolution was obtained along the airplane flight track (taking into account the aircraft speed). Digitization rate was 50 MHz, corresponding to a range resolution of 3.5 m.

System limitations include uncontrolled changes in the pulse shape which made measurements in the first 300 to 400 m impossible, and along pulse width (several microseconds), so that information about the shape of the cloud return is very difficult to obtain. Therefore, for this particular day with low clouds, no reliable cloud base height could be obtained when the aircraft was flying close to the ocean surface underneath the cumulus and broken cloud region. Our method of analysis consisted of examining each individual profile and identifying the range of maximum cloud top return. The signal was then searched backward until a range of heights was obtained where the signal did not change much. Actual cloud height was chosen as the height at which the signal level above the constant background was 10% of the difference between the constant (background) value and the maximum cloud return. Figure 7 shows the cloud heights on the only east–west flight leg (flown at 850 hPa) for which reliable measurements could be obtained. Clearly visible is the breakdown of the solid stratocumulus deck with small altitude variability (700–750 m: 936–930 hPa) in the east, to the broken clouds and finally very small cumulus clouds with high altitude variability towards the west. These had tops in the range 400–600 m (971–948 hPa). We estimate from lifting condensation levels (LCLs) in the subcloud layer that the small cumulus clouds had bases near 971 hPa (400 m). To the far west the cumulus clouds disappear in the clear region, as the tops drop to 400 m (971 hPa). A 60-point smoother was applied to the data; this appears in the graph as a solid line through the cloud height data. The distinct change in average cloud top height, with the high clouds in the east and the lower clouds in the west, is associated with a fall in the height of the inversion base (see Fig. 8, later). The bottom curve on Fig. 7 represents the cloud fraction based on a 60-shot running mean of the cloud heights, roughly corresponding to a 10 km average.

Under the stratocumulus the lidar gave a reliable cloud base for the two 1010 hPa runs. From 1921 to 2146 UTC, the mean stratocumulus cloud base as measured by lidar (which was uniform on the 10 km scale within ± 10 m) lifted 100 m from 520 to 620 m (not shown). The corresponding LCLs measured by aircraft just below cloud base lifted a little less from 958 to 952 hPa (510 to 555 m). This cloud base lifting appears consistent with some decoupling between the cloud layer and the surface layer near local noon; since over the same time period, the LCL at 1010 hPa *dropped* from 966 to 976 hPa. Correspondingly, the subcloud gradient of p^* with p increases, indicating a less well mixed structure (see Fig. 11, later).

4. Averaging of data into cloudiness regimes

The boundary between the cumulus and stratocumulus regimes was moving slowly eastward throughout the time of the Electra flight. We used observer's notes on the aircraft as well as the lidar on the aircraft to give an estimate of the mean velocity of the boundary of 3 m s^{-1}. Four regions were identified according to the observed cloudiness which we will refer to as Clear, Cumulus, Broken and Stratocumulus. Clear refers to the far western area where no clouds were present. Only a small fraction of the flight time was spent in this area (two vertical profiles through the boundary layer and parts of the horizontal legs). Cumulus refers to the region where small cumulus clouds were visible, with tops between 400 and 500 m (Fig. 7), but before the clouds developed into larger cells. Broken refers to the transition region between the Cumulus and Stratocumulus where the fractional cloudiness varied between 30% and 95%. Stratocumulus refers to the region towards the east where very few holes appeared between clouds and the boundary layer was almost overcast (Fig. 7). Approximately equal flight time was spent in the last three regions. Since the transition region was moving towards the east, and we are interested in extracting mean thermodynamic profiles with respect to this moving region, the four cloudiness regions were defined as drifting with the (west–east) speed of the average cloud boundary of 3 m s^{-1}. We binned the data into the four cloudiness regimes using these moving longitude boundaries. Table 2 gives the longitude of the boundaries between the different regions at 2032 UTC, the midpattern time. We averaged the data of the main east–west flight legs and profile runs in pressure interval bins of 5 hPa for each of the four cloudiness regimes. The four average profiles are given in Appendix B. Other possible averaging methods such as binning in saturation pressure intervals or liquid water potential temperature intervals (Boers and Betts 1988) were not chosen since most of the vertical variability is isolated by the pressure averaging; and most of the horizontal variability is isolated by our separation of data into the four regions. The 5 mb averaging does produce some smoothing through the inversion, which slopes upward from the clear to the stratocumulus region. Our averaging procedure does not eliminate variability due to
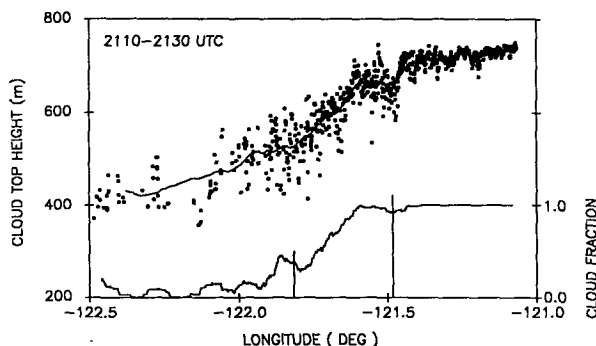

FIG. 7. Lidar cloud top heights (top part of figure) and cloud fraction (bottom part of figure). The vertical lines are the broken cloud boundaries at 2120 UTC, as defined in section 4.

TABLE 2. Boundary between four regions
at 2032 UTC and 31.6°N.

Region	Longitude of boundary (°W)
Clear	
	122.64
Cumulus	
	121.91
Broken	
	121.57
Stratocumulus	

diurnal effects, advection or horizontal inhomogeneities in the atmosphere due to the drift of the atmospheric column over regions of sea surface temperature gradients. Although all of these influences may play a role in modifying the mean structure over time, our averaging technique highlights most of the horizontal variability in the mean structure associated with the thermodynamic transition between a cloud free to cloud covered layer.

a. Thermodynamic and wind profiles

Figure 8 has four panels showing the average vertical profiles of potential temperature and dewpoint (as a

potential temperature) through the CBL. There is a systematic trend with increasing cloud fraction and several features can be seen clearly. With the transition from cloud free to stratocumulus regimes [panels (a) to (d)], the CBL deepens and, as would be expected, becomes moister until it is saturated in its upper layers. The inversion base lifts from 962 hPa (cloud-free) to 932 hPa (stratocumulus), and the inversion becomes much stronger. The thermodynamic structure above the inversion shows dramatic differences. There is a tongue of very dry air immediately above the clear region, and this is capped by a moist layer above. The moist layer disappears with the transition to stratocumulus, leaving dry air above the CBL. Clearly there is an east–west discontinuity in the airmass characteristics near 900 hPa.

Figure 9 shows the corresponding change in the mean wind profiles. These are a little noisier, but they also show significant gradients. The low level wind speed (50 m above the surface) increases from 8.5 to 14 m s^{-1} from the cloud free to stratocumulus regimes (see also Fig. 6c), and the shear reverses with height. The tongue of dry air above the clear region is associated with strong northeasterly flow, which has become northerly over the cumulus, and shifted to weaker northwesterly flow over the stratocumulus. The vertical profiles show some spikes, both because the vertical
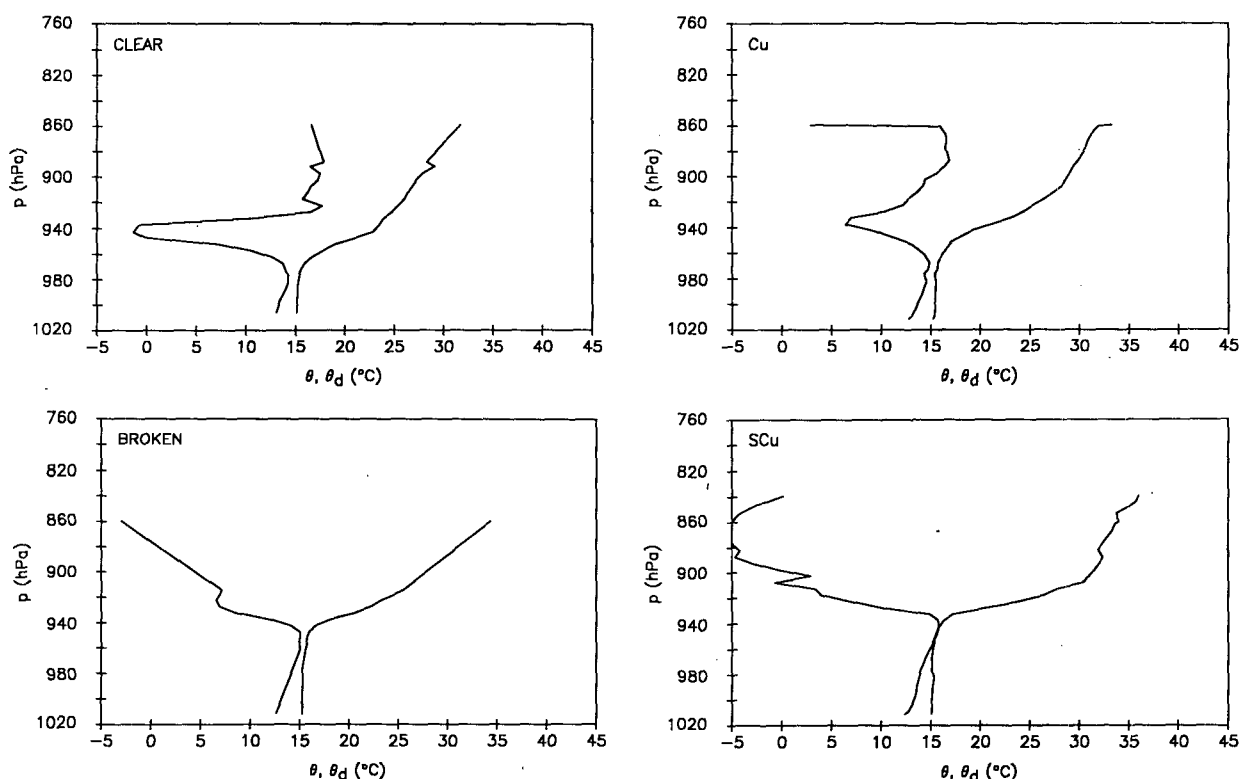

FIG. 8. Mean thermodynamic profiles for four regimes: clear, cumulus, broken, stratocumulus.
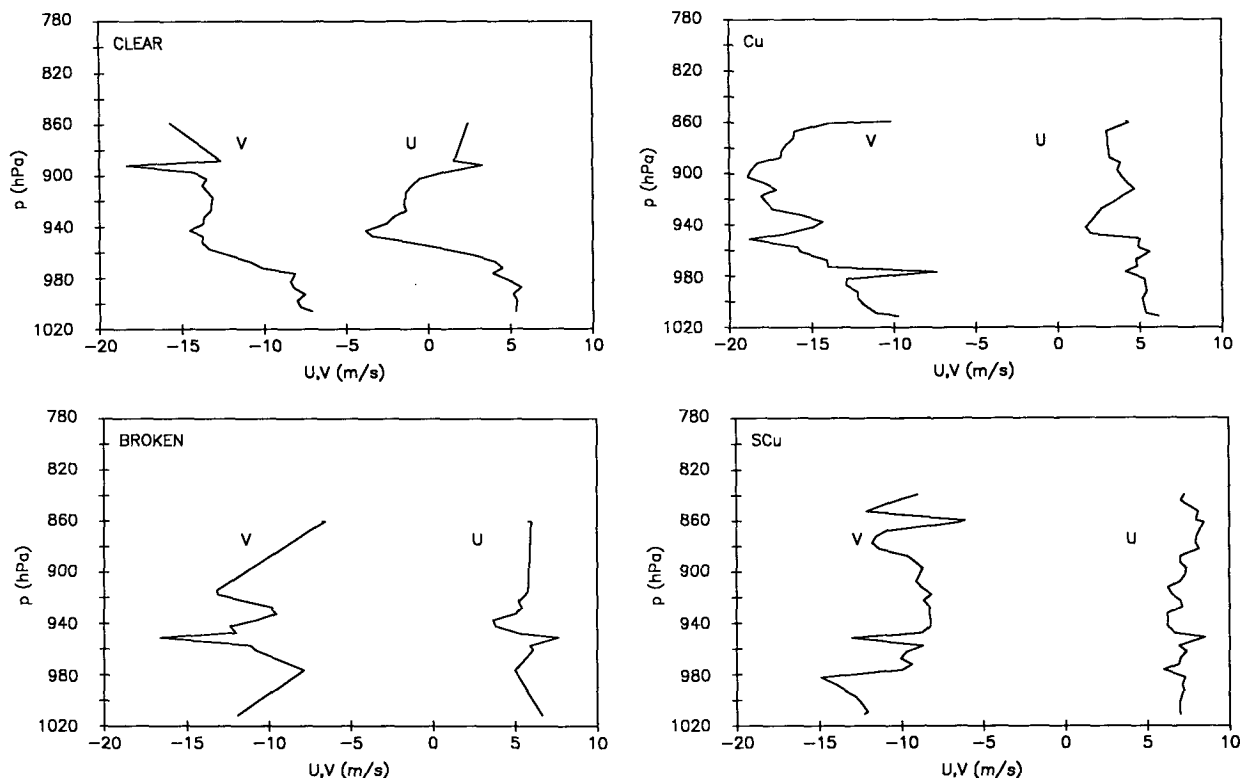
FIG. 9. Mean wind profiles for four regimes: clear, cumulus, broken, stratocumulus.

sampling is not homogeneous and the flow is changing with time (see Fig. 6c).

b. Saturation level structure

Figure 10 shows four panels for the change in saturation level, p^*, with pressure, p, for the averages. The deepening of the CBL from clear to stratocumulus is readily visible. For the clear case the steeper fall of p^* in the inversion has started before the pressure of the maximum of p^* is reached (975 hPa just above the surface). For the cumulus case, the sharp fall of p^* starts about 10 hPa above the highest p^* (again 975 hPa) which is indicative of cloud base. The subcloud layer is not well mixed ($\beta = dp^*/dp = 0$) for any of the averages, and there are variations of the gradient of β in the subcloud layer: with values of $\beta = 0.45$, 0.32, 0.36, and 0.37 for the clear, cumulus, broken and stratocumulus averages respectively. The cloud-free boundary layer is the least well mixed (larges β). $\beta \approx 0.4$ is a representative value as well for the stratocumulus *cloud layer*. Boers and Betts (1988) found a similar value of $\beta \approx 0.4$ for a stratocumulus layer off the west coast. There is a kink in the mean $p^*(p)$ profile for the stratocumulus near 980 hPa. The lidar (section 3e showed a lifting of cloud base from 520 to 620 m (956 to 944 hPa) during the flight pattern, whereas p^*

for the 1010 hPa leg dropped from 966 to 976 hPa. This suggests that there may be some uncoupling of the stratocumulus layer from the mixed layer due to radiative absorption near solar noon (Nicholls 1984; Nicholls and Leighton 1986). We partitioned the data for this region into early and late time blocks, each 2 hours in length (although the time sampling in these averages is not homogeneous). Figure 11 shows that the gradient of saturation pressure for the whole CBL increases from $\beta \approx 0.20$ to ≈ 0.44 from the early to late averages, suggesting again that the vertical coupling between cloud and subcloud layers has decreased. Betts (1990) found similar behavior in the diurnal variation of stratocumulus over San Nicolas Island.

c. Conserved variable diagrams

Figure 12 shows the four thermodynamic profiles on a conserved variable plot of saturation potential temperature, θ^* against total water q^* (Boers and Betts, 1988). Below cloud base one can see a profile of saturation point (Betts 1982, 1985) nearly parallel to the dry virtual adiabat (constant θ_v^*) for all the profiles (see enlarged section in Figs. 12a,b, and d), as found by Betts and Albrecht (1987). Above cloud-base and through the inversion, a nearly linear mixing line profile with a characteristic slope can be seen. The wet virtual
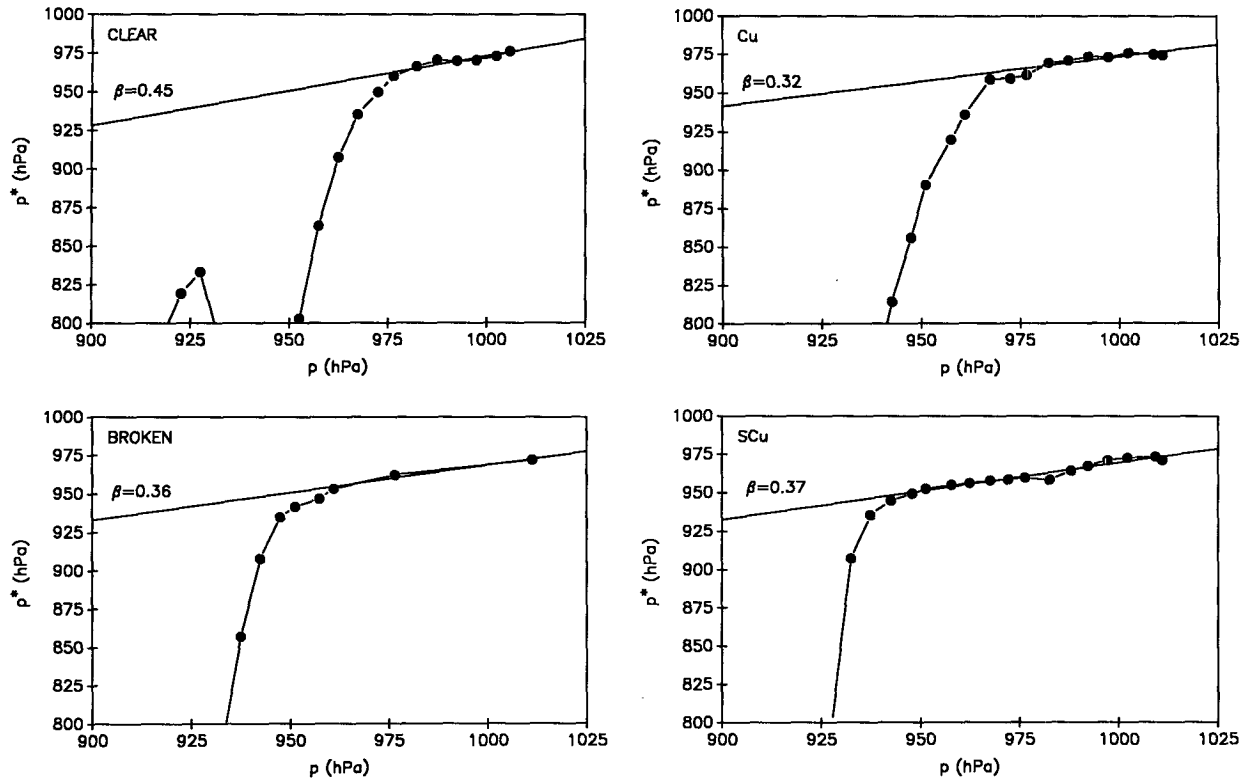
FIG. 10. Profile of p^* against pressure for four regimes.

adiabat $\theta^*_{ev} = 310$ K is shown. There is a clear progression of the *stability* of the mixing line with cloud fraction. Because of the relatively cool and dry tongue of air above the cloud-free and cumulus CBLs, the mixing line profile through the CBL is *very unstable* to the wet virtual adiabat in Figs. 12a, b. However, the profile through the stratocumulus, with a much warmer overlying inversion is close to neutral with respect to a wet virtual adiabat, although it is still marginally unstable.
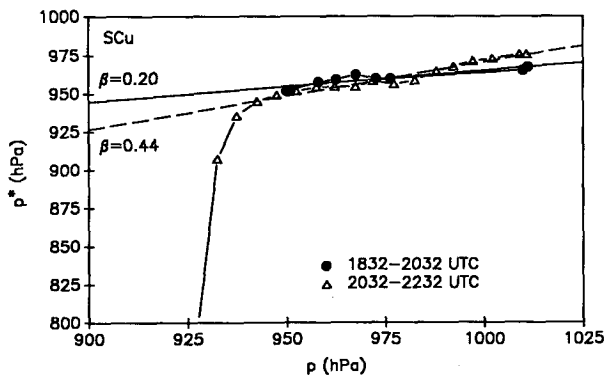
FIG. 11. Profile of p^* (p) for stratocumulus for early and late time averages.

d. Cloudiness transition and the CTEI criterion

The wet virtual adiabat represents the stability criterion (Betts 1983) for cloud-top entrainment instability (CTEI), which was suggested as one mechanism for the breakup of stratocumulus by the unstable downward mixing of inversion level air (Randall 1980; Deardorff 1980). There has been considerable discussion as to whether CTEI is a sufficient condition for the breakup of stratocumulus (Hanson 1984; Albrecht et al. 1984; Randall 1984; Nicholls and Turton 1986; Rogers and Telford 1986; Kuo and Schubert 1988; Siems et al. 1990; and others). Betts (1985) suggested that instability with respect to the wet virtual adiabat, together with cloud liquid water content, give a measure of the velocity scale associated with the downward mixing of dry air through cloud-top entrainment. Figure 12 suggests that, although instability with respect to the wet virtual adiabat is not a sufficient criterion for stratocumulus breakup, it is still an important reference process for the transition between cumulus and stratocumulus boundary layer. The mixing line profile through the cumulus layer is very unstable to the wet virtual adiabat whereas through the stratocumulus, it is nearly neutral (albeit slightly unstable). Can we establish a relationship between cloud fraction and mixing line slope using this data? Cloud fraction was measured on one cross section on the airborne lidar (Fig.
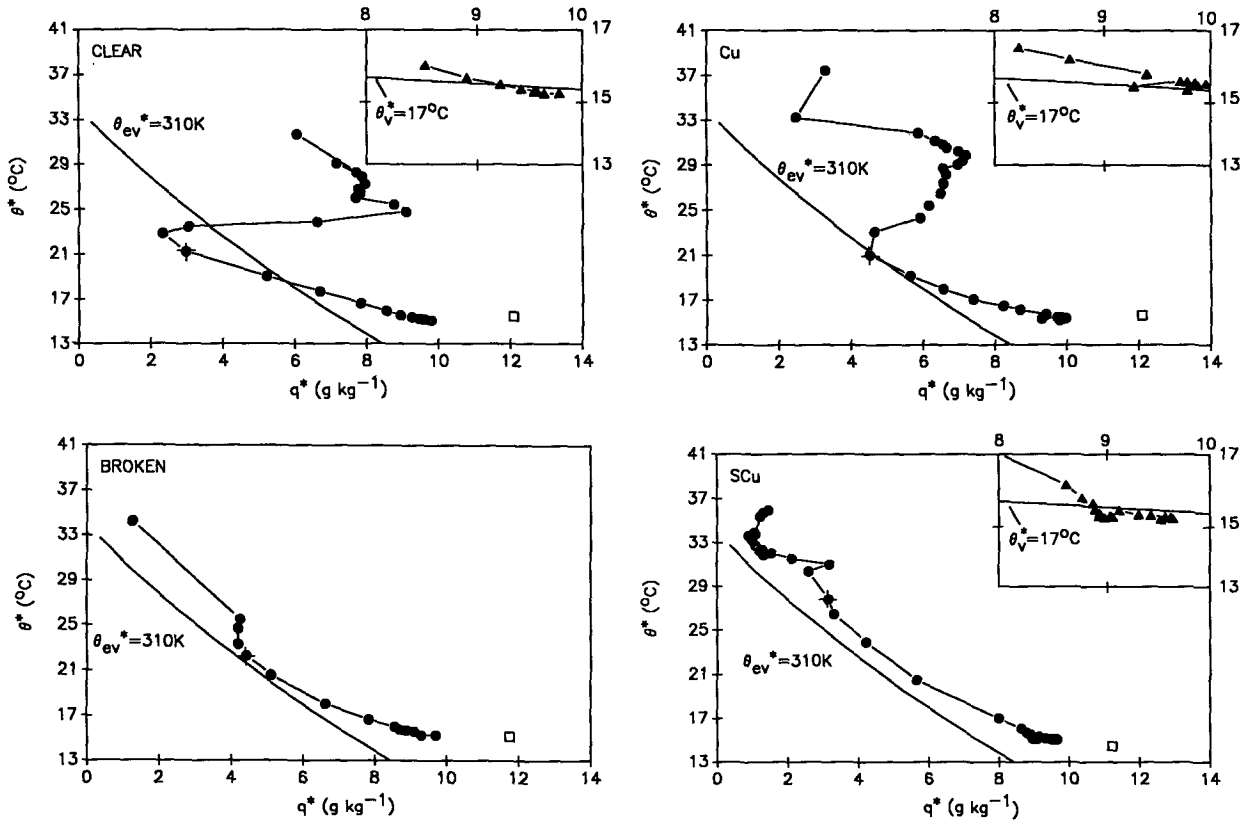
FIG. 12. Conserved variable plots (θ^*, q^*) showing profiles for four regimes.

7). From visual observations we know the change with time was small. The (θ, q) profiles through the CBL are slightly curved in Fig. 12 (in part because of the averaging), so we defined a mean slope by fitting a linear regression line through the cloud layer from the data level below cloud base to the (θ, q) points marked by cross-hairs in Fig. 12. These slopes are shown in the first column of Table 3. The standard error of the coefficients of the linear fit are given. The selection of the points marked by cross-hairs deserves discussion. The break in the quasi-linear mixing line profile, indicating the limit of convective mixing in the boundary layer (Betts 1985), is unambiguous for the clear, cumulus and broken profiles. For the clear case, for example, we might choose to include in the regression one higher level data point corresponding to the q minimum, but this will clearly bias the linear fit to a higher slope (with a larger standard error). For the stratocumulus case, the limit of convective mixing is less clear, as the top of the sharp inversion is two data points higher (just below an increase in q). If we include these two additional points in the line fit, the slope increases to a value close to that of the wet virtual adiabat. The instrumental uncertainties introduce further possible errors in the slopes, but these are hard to assess, since we have no information on the height dependence of any instrumental biases.

Table 3, column 1, also shows the mean slopes of the dry and wet virtual adiabats (see Appendix A) and the wet adiabat; and in columns 2 and 3, the mixing line slopes normalized by ($\partial\theta^*/\partial q^*$) for the wet adiabat and the wet virtual adiabat. The fourth column gives the mixing line slopes in (θ^*, p^*) coordinates again normalized by the slope of the wet adiabat. The last column gives cloud cover for the four cloudiness regimes. The transition from stratocumulus to cumulus (the broken cloud case) occurs at a normalized mixing line slope of

$$\Gamma_m/\Gamma_{wv} = 0.66 \pm 0.04 \qquad (2a)$$

only two-thirds of the slope of the wet virtual adiabat in the (θ^*, q^*) coordinate system. Table 3 gives other representations of this threshold in terms of the wet adiabat

$$\Gamma_m/\Gamma_w = 0.53 \pm 0.03 \qquad (2b)$$

and (θ^*, p^*) coordinates

$$(\partial\theta^*/\partial p^*)_m/(\partial\theta^*/\partial p^*)_{\theta_c^*} = 0.71 \pm 0.04. \qquad (2c)$$

This transition in cloudiness is climatically important, and it clearly occurs on the unstable side of the CTEI threshold (Γ_{wv}) as noted by other authors (cited

TABLE 3. Mixing line slopes for four cloudiness regimes, and the virtual adiabats.

	$\Gamma = \partial\theta^*/\partial q^*$ [K (g kg^{-1})$^{-1}$]	Γ/Γ_w	Γ/Γ_{wv}	$(\partial\theta/\partial p)_m/(\partial\theta^*/\partial p^*)_{\theta_i^*}$	Cloud fraction (%)
Dry virtual adiabat	-0.18	0.085			
Clear	-0.95 ± 0.01	0.36 ± 0.01	0.45 ± 0.01	0.52 ± 0.01	0
Cumulus	-1.03 ± 0.08	0.39 ± 0.03	0.49 ± 0.04	0.60 ± 0.04	12
Broken	-1.39 ± 0.08	0.53 ± 0.03	0.66 ± 0.04	0.71 ± 0.04	73
Stratocumulus	-1.85 ± 0.07	0.70 ± 0.03	0.87 ± 0.04	0.83 ± 0.04	99
Wet virtual adiabat	-2.11	0.80	1	0.9	
Wet adiabat	-2.63	1	1		

earlier). In the case we have analyzed, the highly unstable thermodynamic structure on the cumulus side arises because the inversion is much weaker so that the air above the inversion is relatively cool—not from the modest increase in SST nor from any large change in mixing ratio above the inversion.

Kuo and Schubert (1988) analyzed all the FIRE soundings on San Nicolas Island in terms of stability and cloud cover. The stability criteria $\Gamma_m/\Gamma_w \approx 0.53$ corresponds to $\Delta\theta_e = (\theta_e/T)(1 - 0.53)(L\Delta q/C_p) \approx 0.53(L\Delta q/C_p)$ on their Fig. 4. Only one (out of 55) of their data points for solid stratocumulus lies on the unstable side of this threshold. Similarly most (41 of 47) of their stratocumulus data from a much larger dataset on their Fig. 1 also lie on the stable side of this threshold. This stability threshold for the stratocumulus–cumulus transition, on the unstable side of the CTEI criterion, is in general agreement with Siems et al. (1990), who suggest that weak instability with respect to the CTEI criterion should simply enhance entrainment, rather than cause explosive entrainment and the rapid breakup of the cloud layer. MacVean and Mason (1990) discussed the instability of two layers straddling cloud top, one cloudy and the other clear, and derived (for layers of equal thickness) a threshold, $\Delta\theta_e \approx 0.7(L\Delta q/C_p)$, which is somewhat more unstable than our empirical value.

e. Parameterization of CBL cloudiness

Equation (2) suggests a new empirical criterion for stratocumulus breakup. Results from a single case study such as this should be treated with caution, since our analyses cover a three hour time period, and we have no in situ data on the time history of this cloud field or the effects of upstream advection. We have observed an east–west transition in structure between the cloudiness regimes, but the dominant advection is from the north-northwest, roughly parallel to the moving stratocumulus boundary. Nonetheless, we consider the possibility that mixing line slope might form the basis for a simple parameterization of cloud fraction in global models. This could be combined with the simple ad-

justment parameterization for shallow cumulus transports using a mixing line slope, as proposed by Betts (1986). In Fig. 13 we plot cloud fraction against mixing line slope. The lower x-axis is $\Gamma_m = (\partial\theta^*/\partial q^*)_m$ normalized by the wet adiabat, and the upper is normalized by the wet virtual adiabat. We present both, because although the wet adiabat normalization may be more familiar, it is instability with respect to the wet virtual adiabat that supplies energy for the downward mixing of inversion-level air in cloudy mixtures (Betts 1985). The two dotted vertical lines represent the slopes of the dry and wet virtual adiabats, the stability criteria for unsaturated and cloudy air motion. The solid circles are the 7 July FIRE data from Table 3, which were analyzed in the previous section. The open square, marked PLANET, is an average of 12 boundary layer soundings from the Research Vessel Planet during the Atlantic Trade-Wind Experiment (ATEX) (Augstein et al. 1974; Betts and Albrecht 1987), for which the mean cloud fraction was 50%, based on visual cloud estimates in octas. The open circles are three averages from the 1972 Venezuela International Meteorological and Hydrological Experiment (VIMHEX), where vi-
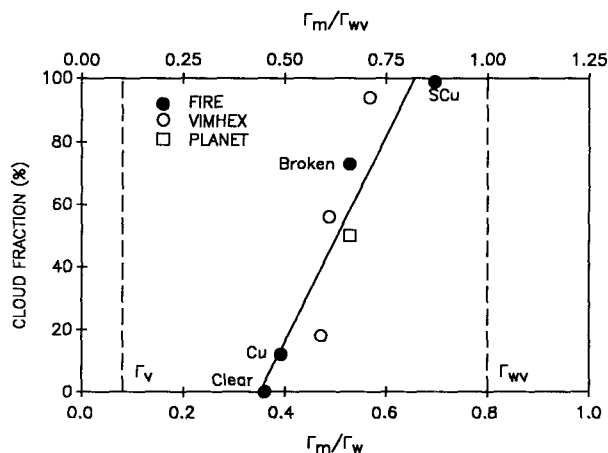

FIG. 13. Cloud fraction as a function of mixing line slope.

sual estimates of shallow cumulus cloud fraction were available in three broad classes (roughly corresponding to 1–2 octas, 3–6 octas and 7–8 octas). There are 25, 89 and 10 soundings respectively in the three averages going from low to high cloud cover. These soundings were collected in convective conditions (without precipitation) during the daytime over land (Betts 1976). They also show mixing line stability increasing with boundary layer cloud cover. The general agreement (considering the uncertainties in mean cloud cover of order 10%–20%) with the oceanic transition between cumulus and stratocumulus on 7 July 1987, is encouraging. We have added the dashed regression line on Fig. 13 to suggest a simple parameterization for the climatic transition from stratocumulus to cumulus, suitable perhaps for some global models.

cloud fraction

$$= (0.5 \pm 0.16) + (2.6 \pm 0.5)(\Gamma_m/\Gamma_{wv} - 0.63)$$

$$= (0.5 \pm 0.18) + (3.2 \pm 0.6)(\Gamma_m/\Gamma_w - 0.49). \quad (3)$$

The error estimates are from the fit of the linear regression line, with a correlation value of 0.84. There are many factors which we have not addressed. A subtle balance of convective and radiative transports, surface forcing and the entrainment of dry air from above probably controls the small cloud fraction in shallow cumulus fields (Betts and Ridgway 1988), so it is likely that the simple linear fit in Fig. 13 is inadequate as a prediction of *small cloud* fraction. Betts and Albrecht (1987) presented data for other average tradewind cumulus datasets for which no estimate exists for cloud fraction. Their shallow CBLs, with inversion tops no deeper than 800 hPa showed a single mixing line and a range of normalized slopes (Γ_m/Γ_w) from 0.3 to 0.4. Their deeper boundary layers generally showed a double mixing line structure with correspondingly more stable values of Γ_m/Γ_w in the range 0.4 to 0.5 coinciding perhaps with multiple cloud decks. While these values are generally consistent with Fig. 13, they indicate the complexity of the prediction of cumulus cloud fraction. For stratocumulus, there are also other processes involved. For example, at the analysis time near local noon 7 July the stratocumulus appeared to be thinning through the rise of cloud base, as it was destabilized by radiative cooling at cloud top and warming at lower layers in the cloud. At another extreme, in the presence of large surface fluxes producing strong mixing the transition to stratocumulus may take place for a more unstable mixing line. We note also that our estimates of mixing line slope from cloud base to cloud top use data with high vertical resolution (from 6–18 levels in the cloud layer), whereas global models have typically much poorer vertical resolution from which to estimate mixing line slope. Clearly there are many other factors that need further study to give an accurate prediction of cloud fraction.
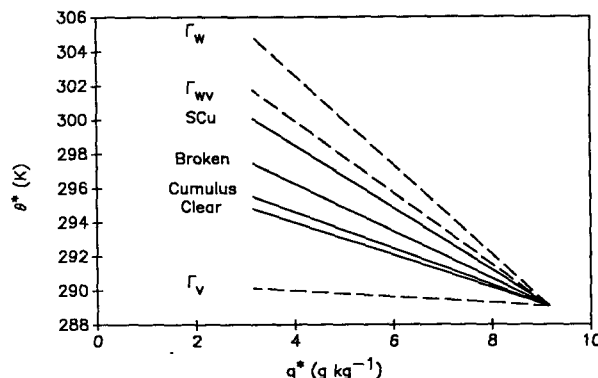

FIG. 14. Cloud regimes and adiabats on a (θ^*, q^*) plot.

5. Discussion and conclusions

This transition in wind and thermodynamic structure associated with this transition in cloudiness from a clear sky through tiny cumulus, broken stratocumulus to a solid stratocumulus deck is fascinating. It is rare that we have this detailed information in conjunction with satellite pictures so we have presented the profiles in Appendix B. This cloud transition had a long north–south extension, and could be traced back in time on satellite pictures (Kloessel 1989, personal communication). It appears to be associated with a change in the inversion structure. Above the cumulus, the inversion is lower but much weaker in strength, and the air above still quite dry, so that the mixing line through the cloud layer is very unstable to the wet virtual adiabat; thus, there is considerable energy available for the downward mixing of dry air. Above the stratocumulus, the much stronger inversion gives rise to a mixing line which is only marginally unstable to the wet virtual adiabat, apparently not enough to break up the solid cloud layer in the face of mixing driven by radiative destabilization and shear generation at the surface. Figure 14 summarizes on a (θ^*, q^*) plot the transition in mixing line slopes we observed in relation to the transition in cloud fraction, and the transition in stability between the dry and wet virtual adiabats. The dry adiabat is parallel to the q-axis and the wet adiabat is the line with steepest slope. One mean slope has been plotted for the slightly curved wet virtual adiabat (the value used in Table 3). Betts (1982) first proposed that mixing line slope would give a useful categorization of different cloud regimes and their stability, and this study confirms this. We recommend the (θ^*, q^*) plot as a powerful tool to show transitions in stability between different CBL regimes.

The lidar data (Fig. 7) show the transition in cloud fraction and the rise of cloud top from the cumulus to stratocumulus regimes, associated with the thermodynamic changes. Figures 8 and 12 and 14 show a progression from the clear air profiles, where the mixing

down of very dry air (with $q \approx 2$ g k g^{-1}) appears to be sufficient to prevent clouds from forming, to the cumulus regime where clouds developed with a vertical extent of 50–200 m (Fig. 7). Likewise the broken cloud region shows an intermediate thermodynamic structure between cumulus and stratocumulus. From the thermodynamic structure of the broken stratocumulus we made an estimate of the critical mixing line slope for the formation or breakup of the stratocumulus. Expressed in terms of the slope of the wet virtual adiabat, we obtained

$$(\Gamma_m)_{CRIT} = (0.66 \pm 0.04)\Gamma_{wv}$$

$$\text{where} \quad \Gamma = (\partial\theta^*/\partial q^*) \quad (2a)$$

In terms of (θ^*, p^*) and the slope of the wet adiabat

$$(\partial\theta^*/\partial p^*)_m/(\partial\theta^*/\partial p^*)_{\theta^*_e} = 0.7 \pm 0.04. \quad (2b)$$

This threshold corresponded to roughly a 70% cloud fraction. As has been suggested by many authors, this is more unstable than the wet virtual adiabat. This suggests that while evaporative enhancement of entrainment (Siems et al. 1990) may occur on the unstable side of the CTEI threshold, it takes a finite instability to produce cloud breakup. This threshold is in general agreement with the data for stratocumulus summarized in Kuo and Schubert (1988). We plotted cloud fraction against mixing line slope (Fig. 13), found general agreement with average cloud fraction data collected over land in Venezuela and an oceanic average, and suggested a simple linear parameterization of cloud fraction for global climate models. More work is needed on this.

There is some indication in this data that the stratocumulus layer partly uncouples from the subcloud layer near local noon as has been suggested by Nicholls (1984). The stratocumulus cloud base as observed by lidar rises 100 m during the flight pattern, while the LCL of the low level air *increases* by 10 hPa during the same time.

APPENDIX A

Slope of Mixing Lines and Virtual Adiabats on (θ^*, q^*) Diagrams

In this paper we have used (θ^*, q^*) plots to show mixing line profiles in the CBL, and it is helpful to review the slopes of the thermodynamic reference adiabats in this coordinate system.

The dry adiabat (θ^* = constant) is a coordinate axis; while the dry virtual adiabat (Betts 1982) is a line of constant (dry) virtual potential temperature, defined as

$$\theta^*_v = \theta^*(1 + 0.61q^*). \quad (A1)$$

Hence the slope of the dry virtual adiabat is

$$\Gamma_v = (\partial\theta^*/\partial q^*)_{\theta^*_v}$$

$$= 0.61\theta^*/(1 + 0.61q^*) \approx -0.18 \approx -\frac{1}{6}. \quad (A2a)$$

The wet adiabat is a line of constant equivalent potential temperature for which

$$0 = (\delta\theta^*_e/\theta^*_e) = (\delta\theta^*/\theta^*) + (L\delta q^*/C_pT^*) \quad (A3)$$

so that the slope of the wet adiabat is

$$\Gamma_w = (\partial\theta^*/\partial q^*)_{\theta^*_e} = -(L\theta^*/C_pT^*)$$

$$\approx -2.6 \text{ in the lower troposphere since } (\theta^*/T^*)$$

$$= (1000/p^*)^{0.286} = 1.04 \text{ for } p^* = 870 \text{ hPa}. \quad (A4)$$

This relationship is simple because the wet adiabat defines the temperature change produced by condensation of water vapour. Equation (A2a) can then be written as

$$\Gamma_v = \Gamma_w(0.61\epsilon/(1 + 0.61q^*) \approx 0.07 \Gamma_w \quad (A2b)$$

where $\epsilon = C_pT^*/L \approx 0.12$ (see Table A1).

The wet virtual adiabat, a line of constant virtual equivalent potential temperature, θ^*_{ev} takes account of liquid water loading in a cloudy atmosphere. It is the reference adiabat associated with the CTEI criterion and its slope can be written in θ^*, q^* coordinates (Betts 1983) with slight approximation as

$$(\partial\theta^*_e/\partial q^*)_{\theta^*_{ev}} = (L\theta^*_e/C_pT^*)(\alpha + \epsilon)/(1 + 1.61\alpha) \quad (A5)$$

TABLE A1. Slope of virtual adiabats as a function of q^* at 900 hPa.

	q^*				
	1	5	10	15	20
ϵ	.102	.111	.115	.117	.119
α	.022	.099	.191	.281	.373
$(\alpha + \epsilon)/(1 + 1.61\alpha)$	.120	.181	.234	.274	.307
(Γ_{wv}/Γ_w)	.88	.82	.77	.73	.69
(Γ_v/Γ_w)	.062	.067	.069	.070	.071

where $\alpha = T^* \, dq^*/dT^*$. (A5) gives a measure of the difference of the wet virtual adiabat from the wet adiabat. From (A3)

$$(\partial \theta_e^*/\partial \theta^*)_{q^*} = (\theta_e^*/\theta^*) \qquad \text{(A6)}$$

so that the slope of the wet virtual adiabat on a (θ^*, q^*) diagram is, using (A4), (A5) and (A6)

$$\Gamma_{wv} = (\partial \theta^*/\partial q^*)_{\theta_{ev}^*}$$

$$= -L\theta^*/C_p T^* [1 - (\alpha + \epsilon)/(1 + 1.61\alpha)]. \quad \text{(A7)}$$

The coefficient $\epsilon \approx 0.12$, but α is a strong function of saturation mixing ratio, q^*, through the Clausius-Clapyron equation. Hence the wet virtual adiabats have a noticeable curvature on a (θ^*, q^*) diagram (see Fig. 12). Table A1 shows the coefficients in (A7) and the dependence on q^* of the coefficient which multiplies the slope of the wet adiabat $(-L\theta^*/C_pT^*)$ in (A7). The parameters are given at one pressure (900 hPa), but the pressure dependence is weak in the lower troposphere. Note that on a (θ^*, q^*) diagram, the slope of the dry virtual adiabats is almost a constant fraction of the slope of the wet adiabats, but that the ratio varies much more for the wet virtual adiabats. A similar result hold for a (θ_e^*, q^*) diagram with closely related coefficients. If we define

$$\gamma_w = (\partial \theta_e^*/\partial q)_{\theta_e^*} = 0$$

$$\gamma_D = (\partial \theta_e^*/\partial q)_{\theta^*} = L\theta_e^*/C_p T^*$$

then using (A2a), (A5) and (A6) one can show

$$\gamma_{wv}/\gamma_D = (1 - \Gamma_{wv}/\Gamma_w) = (\alpha + \epsilon)/(1 + 1.61\alpha)$$

$$\gamma_v/\gamma_D = (1 - \Gamma_v/\Gamma_w) \approx 0.93.$$

In contrast, on a (θ, p) diagram, the wet virtual adiabat has an almost fixed slope of 90% of the wet adiabat (Betts 1982) whereas that of the dry virtual adiabat is strongly q^* dependent.

APPENDIX B

Mean Profiles for Clear Cumulus, Broken and Stratocumulus Regimes

1. Clear region

p	T	q	u	v
858.9	18.71	6.06	2.45	−15.72
888.2	18.24	7.17	1.59	−12.63
891.8	19.36	7.16	3.32	−18.34
897.3	18.73	7.86	1.02	−14.30
902.3	18.55	7.94	−0.50	−13.50
907.6	18.60	7.76	−0.98	−13.77
912.6	18.66	7.83	−1.35	−13.44
917.5	18.74	7.69	−1.41	−13.14
922.7	18.63	8.76	−1.45	−13.20
927.4	18.45	9.09	−1.33	−13.24
932.5	18.00	6.61	−2.08	−13.65
937.5	18.05	3.04	−2.51	−13.74
942.8	17.89	2.34	−3.81	−14.54
947.3	16.73	2.97	−3.47	−13.77
952.5	14.98	5.21	−1.07	−13.76
957.4	14.12	6.69	1.00	−13.31
962.5	13.50	7.83	2.80	−12.09
967.4	13.21	8.55	4.06	−10.87
972.5	13.28	8.93	4.50	−10.14
976.5	13.43	9.25	3.91	−8.16
982.4	13.78	9.44	4.96	−8.40
987.5	14.16	9.58	5.65	−8.21
992.6	14.57	9.56	5.18	−7.53
997.5	14.95	9.56	5.39	−8.02
1002.5	15.33	9.65	5.34	−7.80
1006.0	15.61	9.79	5.31	−7.13
1018.8	17.01	12.07		

2. Cumulus

p	T	q	u	v
783.0	16.43	3.30	5.12	−8.10
859.3	20.23	2.48	4.23	−10.16
860.4	19.06	5.87	4.32	−13.92
867.2	19.02	6.34	2.98	−16.04
872.5	19.20	6.56	3.05	−16.11
877.6	19.47	6.65	3.06	−16.58
882.4	19.59	6.98	3.11	−16.84
887.7	19.71	7.19	3.14	−16.90
891.8	19.65	7.11	3.84	−18.28
897.6	19.86	6.97	3.65	−18.69
902.5	19.96	6.56	3.92	−18.90
907.9	19.98	6.63	4.27	−17.79
912.5	19.60	6.56	4.67	−17.17
917.4	19.19	6.48	3.97	−18.09
922.6	18.63	6.16	3.42	−17.75
927.7	18.03	5.90	2.67	−17.37
932.6	17.26	4.65	2.39	−15.65
937.6	15.68	4.51	2.05	−14.35
942.5	14.29	5.64	1.70	−15.01
947.4	13.52	6.56	2.00	−16.66
951.2	12.96	7.38	4.98	−18.80
957.6	12.93	8.23	4.90	−15.86
961.2	12.90	8.70	5.60	−15.68
967.6	13.02	9.41	4.76	−14.09
972.7	13.43	9.41	4.81	−14.02
976.9	13.43	9.29	4.12	−7.42
982.5	14.04	9.72	5.25	−12.91
987.4	14.43	9.79	5.36	−12.89
992.4	14.81	9.86	5.42	−12.23
997.6	15.23	9.85	5.14	−12.20
1002.6	15.64	9.96	5.24	−11.83
1008.9	16.09	9.88	5.35	−11.12
1011.2	16.16	9.79	6.10	−9.80
1017.9	17.01	12.09		

3. Broken

p	T	q	u	v
859.7	21.21	1.26	5.82	−6.73
860.0	21.29	1.26	6.01	−6.58
914.5	17.97	4.25	5.80	−13.17
917.5	17.45	4.19	5.64	−13.10
922.5	16.55	4.20	5.21	−11.52
927.5	15.98	4.42	5.41	−9.88
932.5	14.75	5.11	5.06	−9.53
937.5	12.73	6.63	3.69	−10.73
942.4	11.77	7.84	3.83	−12.35
947.4	11.57	8.55	5.12	−12.01
951.3	11.68	8.69	7.65	−16.62
957.4	12.13	8.88	5.92	−11.14
961.0	12.34	9.09	6.09	−10.83
976.6	13.34	9.29	5.00	−7.86
1011.3	16.17	9.69	6.65	−11.91
1017.3	16.56	11.75		

4. Stratocumulus

p	T	q	u	v
839.4	20.88	1.44	7.29	−8.98
843.9	21.10	1.31	7.09	−10.22
845.8	20.99	1.21	7.26	−10.67
852.6	20.11	1.08	8.10	−12.12
859.5	20.92	1.06	7.98	−6.11
861.1	20.77	0.89	8.44	−6.54
867.6	21.03	0.99	8.21	−10.82
872.7	21.05	1.08	8.01	−11.54
877.3	21.08	1.20	7.95	−11.75
882.2	21.16	1.31	8.16	−11.34
887.5	22.09	1.27	7.03	−9.63
892.4	22.26	1.54	7.00	−9.14
897.5	22.25	2.11	7.40	−8.69
902.4	22.19	3.19	7.33	−8.88
907.5	22.06	2.59	7.01	−9.09
912.5	20.05	3.15	6.26	−8.73
917.4	19.16	3.31	6.48	−8.19
922.5	17.15	4.22	7.02	−8.66
927.6	14.28	5.67	7.12	−8.29
932.4	11.49	8.01	6.24	−8.27
937.4	11.00	8.64	6.27	−8.21
942.5	11.00	8.79	6.22	−8.24
947.8	11.27	8.89	6.63	−8.76
951.2	11.38	8.91	8.49	−13.03
957.7	11.73	8.96	6.92	−8.71
962.4	12.02	8.95	7.40	−9.69
967.5	12.41	9.00	7.03	−10.04
972.1	12.83	9.05	6.91	−9.37
976.4	13.15	9.08	6.01	−9.94
982.5	13.87	9.14	7.28	−14.90
988.0	14.21	9.32	7.10	−13.97
992.3	14.53	9.44	7.20	−13.44
997.2	14.91	9.58	7.09	−12.79
1002.2	15.29	9.63	6.95	−12.44
1009.2	15.84	9.65	6.97	−12.05
1011.0	15.96	9.53	7.01	−12.26
1016.4	15.84	11.22		

REFERENCES

Albrecht, B. A., R. Penc and W. Schubert, 1985: An observational study of cloud-topped mixed layers. *J. Atmos. Sci.*, **42**, 800–822.
——, D. A. Randall and S. Nicholls, 1988: Observations of marine stratocumulus during FIRE. *Bull. Amer. Meteor. Soc.*, **69**, 618–626.
Augstein, E. H. Schmidt, and F. Ostapoff, 1974: The vertical structure of the atmospheric planetary boundary layer in undisturbed trade winds over the Atlantic Ocean. *Bound.-Layer Meteor.*, **6**, 129–150.
Betts, A. K., 1976: Modelling subcloud layer structure and interaction with a shallow cumulus layer. *J. Atmos. Sci.*, **33**, 2363–2382.
——, 1982: Saturation point analysis of moist convective overturning. *J. Atmos. Sci.*, **39**, 1484–1505.
——, 1983: Thermodynamics of mixed stratocumulus layers: saturation point budgets. *J. Atmos. Sci.*, **60**, 2655–2670.
——, 1985: Mixing line analysis of clouds and cloudy boundary layers. *J. Atmos. Sci.*, **42**, 2751–2763.
——, 1986: A new convective adjustment scheme. Part I: Observational and theoretical basis. *Quart. J. Roy. Meteor. Soc.*, **112**, 677–692.
——, 1989: Idealized stratocumulus model for cloud layer thickness. *Tellus*, **41A**, 246–254.
——, 1990: Diurnal variation of California coastal stratocumulus from two days of boundary layer soundings. *Tellus*, **42**, 302–304.
——, and B. A. Albrecht, 1987: Conserved variable analysis of boundary layer thermodynamic structure over the tropical oceans. *J. Atmos. Sci.*, **44**, 83–99.
——, and W. Ridgway, 1988: Coupling of the radiative, convective and surface fluxes over the equatorial Pacific. *J. Atmos. Sci.*, **45**, 522–536.
——, and W. L. Ridgway, 1989: Climatic equilibrium of the atmospheric convective boundary layer over a tropical ocean. *J. Atmos. Sci.*, **46**, 2621–2641.
Boers, R., and A. K. Betts, 1988: Saturation point structure of marine stratocumulus clouds. *J. Atmos. Sci.* **45**, 1157–1175.
Cahalan, R. F., and J. B. Snider, 1989: Marine stratocumulus structure. *Remote Sens. Environ.*, **27**, 95–107.
Deardorff, J. W., 1980: Cloud-top entrainment instability. *J. Atmos. Sci.*, **37**, 131–147.
Duchon, C. E., and J. S. Goerss, 1976: Variance spectrum analysis of aircraft dewpoint measurement system noise. *J. Appl. Meteor.*, **15**, 77–93.
Hanson, H., 1984: On mixed layer modelling of the stratocumulus topped marine boundary layer. *J. Atmos. Sci.*, **41**, 1226–1236.
——, 1987: Radiative–turbulent transfer interactions in layer clouds. *J. Atmos. Sci.*, **44**, 1287–1295.
Kloessel, K. A., B. A. Albrecht and D. P. Wylie, 1988: FIRE Marine stratocumulus observations Summary of operations and synoptic conditions. FIRE Technical Report No. 1. Dept. of Meteorology, Penn State Univ., Univ. Park, PA 16802. 191 pp.
Kuo, H-C, and W. H. Schubert, 1988: Stability of cloud-topped boundary layers. *Quart. J. Meteor. Soc.*, **114**, 887–916.
Lilly, D. K., 1968: Models of cloud-topped mixed layers under a strong inversion. *Quart. J. Roy. Meteor. Soc.*, **94**, 292–309.
——, 1989: Two-dimensional turbulence generated by energy sources at two scales. *J. Atmos. Sci.*, **46**, 2026–2030.

Mahrt, L., and J. Paumier, 1982: Cloud top entrainment instability observed during AMTEX. *J. Atmos. Sci.,* **39,** 622–634.

MacVean, M. K., and P. J. Mason, 1990: Cloud-top entrainment instability through small-scale mixing. *J. Atmos. Sci.,* **47,** 1012–1030.

Nicholls, S., 1984: The dynamics of stratocumulus: Aircraft observations and comparisons with a mixed layer model. *Quart. J. Roy. Meteor. Soc.,* **110,** 783–820.

——, and J. Leighton, 1986: An experimental study of stratiform cloud sheets. Part I: Structure. *Quart. J. Roy. Meteor. Soc.,* **112,** 431–460.

——, and J. D. Turton, 1986: An experimental study of stratiform cloud sheets. Part II: Entrainment. *Quart. J. Roy. Meteor. Soc.,* **112,** 461–480.

Randall, D. A., 1980: Conditional instability of the first kind upside-down. *J. Atmos. Sci.,* **37,** 125–130.

——, 1984: Stratocumulus cloud deepening through entrainment. *Tellus,* **36A,** 446–457.

——, J. A. Coakley, C. W. Fairall, R. A. Kropfli and D. H. Lenschow, 1984: Outlook for research on subtropical marine stratiform clouds. *Bull. Amer. Meteor. Soc.,* **65,** 1290–1301.

Rogers, D., 1986: The onset of entrainment instability over the ocean. *Bound.-Layer Meteor.,* **37,** 167–182.

——, and J. W. Telford, 1986: Metastable stratus tops. *Quart. J. Roy. Meteor. Soc.,* **112,** 481–500.

Schwiesow, R. L., 1987: The NCAR airborne infrared lidar system (NAILS), design and operation. NCAR Technical note 291+1A, June 1987, 38 pp. NCAR, P.O. Box 3000, Boulder, CO 80307.

Schubert, W. H., J. S. Wakefield, E. J. Steiner and S. K. Cox, 1979: Marine stratocumulus convection. Part I: Governing equations and horizontally homogeneous solutions. *J. Atmos. Sci.,* **36,** 1286–1307.

Siems, S. T., C. S. Bretherton, M. B. Baker, S. Shy and R. T. Breidenthal, 1990: Buoyancy reversal and cloud-top entrainment instability. *Quart. J. Roy. Meteor. Soc.,* **116,** in press.